HHS Public Access

Author manuscript

Cell Rep. Author manuscript; available in PMC 2021 March 17.

Published in final edited form as:

Cell Rep. 2019 June 04; 27(10): 2799–2808.e3. doi:10.1016/j.celrep.2019.05.018.

Individual oligodendrocytes show bias for inhibitory axons in the neocortex

Marzieh Zonouzi[1,4,*], **Daniel Berger**[2,*], **Vahbiz Jokhi**[1], **Amanda Kedaigle**[1,3], **Jeff Lichtman**[2,†], **Paola Arlotta**[1,3,5,†]

[1]Department of Stem Cell and Regenerative Biology, Harvard University, 7 Divinity Avenue, Cambridge, MA 02138, USA

[2]Department of Molecular and Cellular Biology and Center for Brain Science, Harvard University, 52 Oxford Street, Cambridge, MA 02138, USA

[3]Stanley Center for Psychiatric Research, Broad Institute of MIT and Harvard, Cambridge, MA, USA

[4]Present address: Boehringer Ingelheim, Germany

[5]Lead Contact

Summary

Reciprocal communication between neurons and oligodendrocytes is essential for the generation and localization of myelin, a critical feature of the central nervous system. In the neocortex, individual oligodendrocytes can myelinate multiple axons; however, the neuronal origin of the myelinated axons has remained undefined, and while largely assumed to be from excitatory pyramidal neurons, it also includes inhibitory interneurons. This raises the question of whether individual oligodendrocytes display biases for the class of neurons that they myelinate. Here, we find that different classes of cortical interneurons show distinct patterns of myelin distribution starting from the onset of myelination, suggesting that oligodendrocytes can recognize the class identity of individual types of interneurons that they target. Notably, we show that some oligodendrocytes disproportionately myelinate the axons of inhibitory interneurons, while others primarily target excitatory axons, or show no bias. These results point towards very specific interactions between oligodendrocytes and neurons, and raise the interesting question of why myelination is differentially directed towards different neuron types.

Keywords

Oligodendrocyte; myelination; interneuron; neocortex

[†]Co-corresponding authors: Correspondence: paola_arlotta@harvard.edu and jeff@mcb.harvard.edu.
[*]These authors contributed equally

Author Contributions

All authors contributed to the design of experiments. MZ and DB conducted all the tracing experiments. VJ and AK performed the molecular analysis. PA, DB, MZ and VJ wrote the manuscript with input from all authors.

Declaration of Interests

The authors declare no competing interests.

Introduction

Communication between oligodendrocytes and neurons during cerebral cortex development is critical to establish and maintain neuronal myelination (Gibson et al., 2014), but little is known about these interactions and how they produce the myelin distribution observed in the adult neocortex. Individual oligodendrocytes extend all of their processes to their target axons within a short time frame (Czopka et al., 2013; Watkins et al., 2008), and can myelinate multiple small and large diameter axons (Butt et al., 1998; Friedman et al., 1989; Remahl and Hildebrand, 1990). However, within this framework, the neuronal origin of the myelinated axons and the selectivity with which oligodendrocytes myelinate specific neurons and axons are unknown. This is likely a complex process, since in addition to long-distance excitatory pyramidal neurons, locally-connected inhibitory cortical interneurons are also myelinated (Martin and Whitteridge, 1984; McGee et al., 2005; Peters and Proskauer, 1980), a fact that has received some recent attention (Micheva et al., 2016; Stedehouder et al., 2017; Schmidt et al., 2017). In addition, not all neurons are myelinated equally; for example, we previously showed that myelination patterns of pyramidal neuron axons vary by the laminar location of the neuron (Tomassy et al., 2014). Together, these prior findings indicate that myelination maps in the neocortex are complex and likely the result of highly orchestrated interactions between neuronal classes and myelinating oligodendrocytes. The specificity and temporal dynamics of such interactions remain largely unknown. Here, we report that specific cortical interneuron classes interact differently with oligodendrocytes to adopt subtype-specific myelination features, and, further, individual oligodendrocytes exist in the neocortex that are biased for the myelination of inhibitory interneurons. These data highlight highly specific neuron-oligodendrocyte interactions occurring at the single-neuron level that shape the distribution of myelin along different types of axons in the neocortex.

Results

Cortical interneurons develop class-specific myelination patterns

To gain insight into the origin of myelination patterns of single neurons of the neocortex, we traced axons and myelin ensheathment of inhibitory interneurons, as their myelination is under-studied compared to excitatory pyramidal neurons. We examined their myelination profiles in adult mouse V1 cortex using a large-scale, publicly available electron microscopy dataset which spans 450×350×54 μm^3 from layer I to upper layer IV (Bock et al., 2011). We identified and traced 28 interneurons (Figure 1A) using accepted morphological and synaptic connectivity criteria (DeFelipe et al., 2013; Jiang et al., 2015; Wang et al., 2004), such as the presence of aspiny or sparsely spiny dendrites, which received numerous shaft synapses; dense axonal arborization patterns largely ascending towards the pia; the formation of symmetrical axo-dendritic, axo-somatic, and axo-axonic synapses with pyramidal neurons and other interneurons; and multipolar, bitufted or bipolar dendrites (Figure S1). 22 of the traced neurons displayed non-uniform and variable myelin distribution along their axons. No myelin was detected on the other 6 cells (Figure S2 **cells 23–28**). We could classify 12 of the 28 neurons based on structural traits (**see** Methods) (Petilla Interneuron Nomenclature Group et al., 2008). 7 of these neurons had morphological and synaptic connectivity profiles reminiscent of basket cells (Figure 1B, Figure S2 **cells 1–7)**, 1

appeared to be a Martinotti cell (Figure 1C, Figure S2 **cell 8)**, 1 a bitufted cell (Figure S1C, Figure S2 **cell 26**), 1 a bipolar cell (Figure S1D, Figure S2 **cell 23)**, and 2 resembled neurogliaform cells (Figure S1E, Figure S2 **cells 27–28** and Table S1). The remaining 16 interneurons could not be reliably classified into subtypes as we could not trace enough of their axons and synapses within the EM dataset (Figure S2, **cells 9–22** and **24–25**). We found that all 7 neurons with cortical basket cell morphology had primary axons and side branches that were extensively myelinated (Figure 1B, Figure S2, **cells 1–7**). The neuron that appeared to be a Martinotti cell had a partially myelinated axon (Figure 1C, Figure S2, **cell 8**). These results reveal a degree of selectivity with which oligodendrocytes myelinate axons of specific populations of cortical interneurons.

To increase the number of cells for analysis and facilitate distinction between interneuron classes, we examined the visual cortex (V1) of transgenic mice, using confocal microscopy to trace axons and myelin associated with different classes of interneurons. Neurons were genetically labelled by crossing the Ai14 ROSA-tdTomato reporter line (Madisen et al., 2010) to Cre lines (Taniguchi et al., 2011) driven by marker genes labelling different interneuron classes: parvalbumin (PV) to label basket cells, shrub-like cells, horizontally elongated cells and chandelier cells (Inan and Anderson, 2014; Jiang et al., 2015); somatostatin (Sst) to label Martinotti cells and other Sst^+ interneurons (Yavorska and Wehr, 2016); vasoactive intestinal polypeptide (VIP) to label bitufted cells, bipolar cells and double bouquet cells (Peters, 1990; Rudy et al., 2011); and neuronal nitric oxide synthase (nNOS) to label neurogliaform cells (Taniguchi et al., 2011). Mice were sacrificed at P60, coronal sections were immunolabeled for myelin basic protein (MBP), and myelination profiles along axons were reconstructed from confocal stacks (Figure S3A; see Methods). We traced single axons projecting from the cell body or primary dendrites of PV^+, Sst^+, VIP^+, and $nNOS^+$ neurons in layer II/III of V1, following them as far as possible within the confocal stacks (Figure S3A, movie S1; see Methods). We found that all axons traced from the cell bodies of PV^+ cells (75/75 cells, n = 3 animals) and ~1/2 of the axons traced from the cell bodies of Sst^+ cells (15/33 cells, n = 3 animals) were myelinated (Figure S3B). We identified myelin on the axons of a small number of VIP^+ neurons (8/64 cells, n = 3 animals). In contrast, we did not detect any MBP on the axons of $nNOS^+$ neurons, although this dataset allowed us to examine only a small number of these cells (0/6 cells, n = 3 animals) (Figure S3B), and it remains possible that $nNOS^+$ interneurons become myelinated in older animals (>P60). These results are in agreement with recent findings that the majority of PV^+ cortical interneurons are myelinated (Micheva et al., 2016; Stedehouder et al., 2017). However, we now show that large fractions of other interneuron subtypes, including nearly half of Sst^+ neurons, are myelinated. Importantly, we find that interneurons display class-specific differences in longitudinal deposition of myelin along their axons; an interesting parallel to excitatory neurons, where neurons in different laminae present distinct longitudinal myelination profiles (Tomassy et al., 2014).

One possible mechanism for the differences in myelination profiles between different neuronal subtypes could be neuron-class specific modulation of neuron-oligodendrocyte signaling, in which neurons deploy specific molecular “codes” of interacting molecules to communicate with their oligodendrocyte partners. To identify complementary interacting

proteins between neurons and oligodendrocytes that could mediate this process, we examined three distinct molecular datasets. First, we began with a matrisome database (Naba et al., 2012), a collection of proteins that are present on the cell surface or secreted into the extracellular space, which we hypothesized to be the two main categories of molecules most likely involved in neuron-oligodendrocyte interaction. We then used molecular datasets of genes expressed in cortical interneuron subtypes (Tasic et al., 2016) and in all oligodendrocytes (Marques et al., 2016) to select for matrisome molecules that were enriched at least 2-fold in PV^+ neurons (highly myelinated) vs. VIP^+ or $nNOS^+$ interneurons (less myelinated or unmyelinated) and that had corresponding receptors or target interactors in oligodendrocytes (Figure S3E). We identified numerous pairs of interacting proteins between oligodendrocytes and PV^+ interneurons, including several members of the interleukin, serpin, and cathepsin families of cell-signaling molecules. Together the data point at potentially regulated interactions between interneuron types and oligodendrocytes, and proposes a first set of molecules that may contribute to this process.

Interneuron class-specific myelination patterns are present from the onset of myelination

To investigate whether these distinctive, class-specific myelination patterns are constitutive features of specific classes of myelinated neurons, or rather a result of differential refinement later in life (for example by myelin shedding), we investigated whether differences in myelination between interneuron classes were present from the onset of myelination. We traced myelin along the axons of the two major classes of myelinated cortical interneurons, PV^+ and Sst^+ cells, in V1 cortex at P15 (following eye opening and at the onset of myelin deposition), P21 (onset of the critical periods in visual cortex), P30, and P60 (past the end of the critical period; McGee et al., 2005) (Figure 2A,B; see Methods). These two populations were chosen because they are both myelinated, but display clear differences in the extent of axonal myelination. Since some Sst^+ cells also express PV (Hu et al., 2013), we immunolabeled coronal sections from Sst-Cre/*Ai14 ROSA-tdTomato* mice with an antibody against PV, to allow us to identify Sst^+/PV^- cells (Figure 2B). At P15 and P21 limited amounts of myelin across all cortical layers allow tracing of myelinated single axons even in the deep layers. At later ages, high density of myelinated axons in the deep layers makes it difficult to precisely trace single axons; thus, at P30 and P60 we only traced the axons of PV^+ and Sst^+ neurons in the superficial layers.

First, we quantified the total number of PV^+ and Sst^+/PV^- cells with MBP^+ axons at P15, P21, P30, and P60 (Figure 2C). Interestingly, we found that a large fraction of the traced PV^+ axons are already myelinated at P15 (74%; 58/78 cells, n = 5 animals), with a significant increase at P21. After P21, all the traced layer II/III PV^+ axons were myelinated (P21 = 126/131 cells, n = 3 animals; P30 = 111/111 cells, n = 3 animals; P60 = 156/156 cells, n = 3 animals) (Figure 2C). In contrast, we did not detect any MBP signal along individually traced axons of Sst^+/PV^- cells at P15 (0/52 cells, n = 3 animals), and only a small fraction of these neurons were myelinated at P21 (P21 = 19%; 10/52 cells, n = 3 animals). The number of Sst^+/PV^- myelinated axons increased at P30 and P60 (P30 = 58%; 21/36 cells, n = 3 animals; P60 = 52%; 39/75 cells n = 3 animals) but did not reach 100% as observed in PV^+ interneurons (Figure 2C **and** Table S2), indicating that while myelination is a canonical feature of all PV^+ cells, a subset of Sst^+/PV^- neurons appear to myelinate by P60. Given that

during postnatal development myelination progresses from deep to superficial layers over time, we investigated whether differences in myelination of PV^+ cells were associated with layer location. Consistent with the developmental progression of myelin deposition from layers V and VI to upper layer II/III (McGee et al., 2005), at P15, the axons of PV^+ neurons in the lower layers were more extensively myelinated compared to the axons of neurons located in more superficial locations (Figure S3C). However, at P21, all PV^+ interneurons were myelinated to a similar extent, irrespective of their distance from the pia (Figure S3D), suggesting that an individual neuron's myelination pattern is specific to its neuronal subtype and not its position in the cortex.

Because myelin is intermittent along axons (Micheva et al., 2016; Tomassy et al., 2014), we next assessed whether the adult pattern is a product of local myelin shedding during postnatal development. By determining the length of MBP distributed along the length of each of the individually traced axons of PV^+ and Sst^+/PV^- cells, along a timeline from P15 to P60 (Figure 2D), we discovered that axons of PV^+ neurons had higher MBP coverage at all ages (P15 33%±3.04; P21 64.5%±2.0; P30 65.1%±1.45; and P60 64.21%±1.45) compared to the axons of myelinated Sst^+/PV^- cells (P15 0%; P21 9.43%±3.20; P30 32.2% ±6.12; and P60 22.2%±3.50) (Figure 2D). Together, the data indicate that differences in the mature (P60) profiles of myelin distribution along the axons of two different classes of interneurons (PV^+ and Sst^+/PV^-) are present from the very onset of myelin deposition. These data point to the existence of previously unappreciated, highly selective interactions between oligodendrocytes and interneurons that appear to occur early, at the onset of myelination, and may be dependent on specific properties of each interneuron class. We found no evidence of a demyelination process in defining the final distribution of myelinated and unmyelinated axonal segments.

Identification of oligodendrocytes in the mouse visual cortex and their myelinating contacts.

The fact that both pyramidal neurons and a subset of interneurons are myelinated raises the possibility that distinct populations of oligodendrocytes preferentially myelinate particular classes of neurons. To address the neuronal specificity of individual oligodendrocytes, we used the same EM dataset of adult V1 cortex described above (Bock et al., 2011), and identified oligodendrocytes where we could trace multiple branches from their cell bodies to the myelinated target axons (Figure 3A). We found that a single oligodendrocyte can repeatedly myelinate multiple axonal branches of a single cortical basket cell (Figure 3B–C), and, conversely, that multiple oligodendrocytes can myelinate the axon of a single interneuron in layer II/III (Figure 3D).

Subpopulations of cortical oligodendrocytes show individual bias towards myelinating the axons of inhibitory neurons

To address the range of axons an individual oligodendrocyte myelinates, we then attempted to classify each targeted axon as either inhibitory or excitatory, based on previously-established criteria (Table S1). We identified 10 oligodendrocytes where we could classify a minimum of 12 target axons per oligodendrocyte (Figure 3A, Figure 5A). Among these, we found oligodendrocytes that displayed three types of myelination choices. Some

predominantly myelinated axons of excitatory neurons (Figure 4A–C), others were biased for the axons of inhibitory neurons (Figure 4D–F), and, finally, some oligodendrocytes myelinated multiple axons of both kinds (Figure 4G–I). These results suggest previously unappreciated biases by oligodendrocytes for the type of axons that they myelinate in the cerebral cortex.

To explore this further and determine whether individual oligodendrocytes were significantly biased for the types of axons they myelinate, we first traced and estimated the total number of myelinated inhibitory and excitatory axons within a selected volume of V1 (560,303 cubic micrometers). This region was selected because it contained 2 oligodendrocytes (numbers 2 and 5, Figure 3A) with multiple overlapping processes (Figure 5A–B **and** D). We traced a total of 570 myelinated axons in this volume and tried to classify them as either inhibitory or excitatory. Of the axons we were able to classify, 214 (48% of classified axons) were identified as excitatory and 233 (52% of classified axons) as inhibitory. This ratio agrees with previous values obtained from the adult somatosensory cortex (S1) (Micheva et al., 2016). We then used a binomial distribution analysis to determine whether the probability with which the 10 oligodendrocytes myelinated the axons of surrounding inhibitory or excitatory neurons differed from the 48%/52% ratio expected if they targeted local axons at random (Figure 5C). We discovered that while several oligodendrocytes myelinated axons of both excitatory and inhibitory neurons (Figure 5B–C, Figure 4G–I), 4/10 oligodendrocytes were strongly biased towards myelinating inhibitory neurons (oligodendrocytes 4–7) (Figure 5B–C, Figure 4D–F, Figure S4), including two with no identifiable contacts on excitatory axons (oligodendrocytes 4 and 7). Conversely, 1/10 of the oligodendrocytes was significantly biased for myelinating excitatory axons (oligodendrocyte 1) (Figure 5B–C, Figure 4A–F, **and** Figure S5F–H). The remaining oligodendrocytes (5/10) myelinated an approximately equal fraction of inhibitory and excitatory axons (Figure 5B–C, Figure 4G–I, Movie S2, Table S1). Thus, our data indicates that individual oligodendrocytes can display a preference for the class of axons they target; in particular, we find that a large proportion of oligodendrocytes display a strong bias towards myelinating inhibitory axons.

Oligodendrocyte bias towards excitatory versus inhibitory axons is independent of the availability of surrounding excitatory and inhibitory axons.

For the oligodendrocytes that showed preference for excitatory or inhibitory neurons, we sought to understand how this specificity came about. Oligodendrocytes could target axons to myelinate based on their incidental proximity to a neuronal process, or by reciprocal molecular interactions between certain oligodendrocytes and certain axons that encourage or discourage myelination. In an attempt to discriminate between these possibilities, we examined whether oligodendrocytes that were biased towards either inhibitory or excitatory neurons had similar proximity to both populations of axons. We divided the volume of V1 described above into two volumes that immediately surrounded each of the two oligodendrocytes and calculated the total number of myelinated inhibitory and excitatory axons directly surrounding each of the two neighboring oligodendrocytes showing opposing bias (numbers 2 and 5, Figure 5C; in these two volumes we were unable to identify the neuronal origins of ~20% of the axons). We found that while both of the oligodendrocytes

were surrounded by both inhibitory and excitatory myelinated axons, their choice for which class of axon to myelinate was specific and distinct (Figure 5D). Oligodendrocyte 5 showed a strong bias for myelinating inhibitory axons (4 identified excitatory and 22 inhibitory axons) in an environment with slightly more identified myelin sheaths on excitatory than inhibitory axons (52% excitatory and 48% inhibitory axons among those that could be classified), and, conversely, oligodendrocyte 2 showed a strong bias to myelinate excitatory axons (15 identified excitatory and 4 inhibitory axons) in an environment with slightly more myelin sheaths on inhibitory axons (46.2% excitatory and 53.8% inhibitory axons identified). To test the possibility that these ratios are biased by the 20% of axons we were unable to classify, we repeated the analysis shown in Figure 5D and Figure S5I, but assuming that all of the unclassified axons are either inhibitory (Figure S5J) or excitatory (Figure S5K). Under these conditions, oligodendrocyte 5 remains strongly statistically biased to inhibitory axonal targets. Given that these are the most extreme scenarios (all unclassified axons being either all inhibitory or all excitatory), we conclude that it is unlikely that the unclassified axons would change the statistical significance of the biases that we report.

Together, these results indicate that interactions between oligodendrocytes and neurons to produce local patterns of myelination display a previously unappreciated level of specificity acting at the level of individual oligodendrocytes and neurons.

Discussion

Recent data have highlighted complex patterns of myelin distribution along the axons of cortical neurons, and have opened the door to investigate the principles that govern neuron-oligodendrocyte interaction to build maps of myelin distribution found in the adult. Pyramidal neurons in different cortical layers have distinct profiles of myelination along their axons (Tomassy et al., 2014). Similarly, many cortical interneurons are also myelinated, despite making relatively short local connections compared to pyramidal neurons (this study and Micheva et al., 2016, Stedehouder et al., 2017). Importantly, we report here that several other interneuron classes are also myelinated and, notably, display unique profiles of myelin distributions along their axons. The data indicate that the diversity of cortical interneurons and pyramidal neurons contribute to the development of specific myelin placement in the neocortex. These findings shed new light on the role of myelin in circuit functionality, and suggest the possibility that individual neurons may use different strategies to modulate their signaling output.

Myelin distribution along the axons of both inhibitory and excitatory neurons is correlated with, and is possibly dictated by, their class-specific neuronal identity. Myelin-rich PV^+ interneurons differentially express extracellular proteins that have cognate receptors in oligodendrocyte populations, compared to myelin-poor $nNOS^+$ or VIP^+ interneurons, offering an initial support for this hypothesis. The finding that interneurons “define” their class-specific myelination profiles early in cortical development further supports the hypothesis that establishment of neuronal diversity informs early interactions with oligodendrocytes to shape the adult myelin distribution on each neuronal subtype. While this does not exclude the possibility that myelination of each neuronal class is also modulated by

extrinsic factors such as activity and experience, the results suggest that a basic blueprint of the adult map is present from early stages of neuronal development and is dependent on the type of neurons produced.

Individual oligodendrocytes can myelinate multiple axons in the neocortex (Butt et al., 1998; Remahl and Hildebrand, 1990, Osanai et al., 2017); however, the identity of the neurons myelinated by each oligodendrocyte has been difficult to establish. We discovered that the neocortex contains subsets of oligodendrocytes with distinct biases for the type of axons that they myelinate. These included oligodendrocytes that myelinate axons of both excitatory and inhibitory neurons equally, as well as oligodendrocytes that display a bias in the choice of either inhibitory or excitatory axons. Mature oligodendrocytes have been reported to be molecularly heterogenous (Marques et al., 2016); our finding that 40% of the oligodendrocytes in our dataset primarily or exclusively myelinate inhibitory axons raises the possibility that these may represent a distinct subpopulation. While our analysis was limited by the numbers of traceable oligodendrocytes in the EM dataset, our data also indicates the presence of a proportion of oligodendrocytes with a complementary excitatory bias, which further supports the presence of oligodendrocyte classes with unique myelination choices.

Furthermore, our data suggests that oligodendrocytes do not passively accept any axons in their vicinity but instead target axons of specific types, likely through active signals or molecules intrinsic to neuronal subtype which lay out the pattern of myelin distribution in the neocortex. Future work linking target choice to molecular and functional characterization of oligodendrocytes may provide insight into the role of oligodendrocyte heterogeneity in regulating differential myelination in the cortex.

Altogether, these results provide a framework for the interaction between different neuron classes and oligodendrocytes, suggest the possibility that oligodendrocytes may have a currently unappreciated role in modulation of excitatory and inhibitory communication within the cortical circuit, and inform strategies to identify the molecular mechanisms driving these orchestrated interactions.

Methods

CONTACT FOR REAGENT AND RESOURCE SHARING

Further information and requests for resources and reagents should be directed to and will be fulfilled by the Lead Contact, Paola Arlotta (paola_arlotta@harvard.edu).” Any restrictions (e.g., MTAs, data/material linked to sensitive medical information

EXPERIMENTAL MODELS AND SUBJECT DETAILS

Mice—We used the following mouse lines: Plp1-eGFP (Mallon et al., 2002), *Pvalb*$^{tm1(cre)Arbr}$ (PV-Cre) (IMSR Cat# JAX:017320, RRID:IMSR_JAX:017320), *Sst*$^{tm2.1(cre)Zjh}$ (SSt-Cre) (IMSR Cat# JAX:013044, RRID:IMSR_JAX:013044), *Vip*$^{tm1(cre)Zjh}$ (VIP-Cre) (IMSR Cat# JAX:010908, RRID:IMSR_JAX:010908) (with a C57BL/6 background) (Madisen et al., 2010; Taniguchi et al., 2011), and *Nos1*$^{tm1.1(cre/ERT2)Zjh}$/J (nNOS-CreERT2) (IMSR Cat# JAX:014541,

RRID:IMSR_JAX:014541) (with a C57BL/6 background) (Taniguchi et al., 2011). All lines were crossed to the Ai14 ROSA-tdTomato reporter line *Gt(ROSA)26Sor*tm9(CAG-tdTomato)Hze/J (IMSR Cat# JAX:007909, RRID:IMSR_JAX:007909) (Madisen et al., 2010) to visualize the neuronal cell bodies and axons. To induce tdTomato expression in the Nos1-CreERT2 line, mice were injected daily with 5mg 4-hydroxytamoxifen in corn oil for 5 days as described previously (Taniguchi et al., 2011). Both male and female mice were used. All procedures were designed to minimize animal suffering and approved by the Harvard University Institutional Animal Care and Use Committee and performed in accordance with institutional and federal guidelines.

METHOD DETAILS

Fluorescence immunohistochemistry—Immunohistochemistry was performed at P15, P21, P30 and P60 timepoints in mice. Mice were anesthetized with tribromoethanol (Avertin) and transcardially perfused with 0.1 M PBS (phosphate-buffered saline, pH 7.4) followed by 4% paraformaldehyde, as described previously (Arlotta et al., 2005). Cortical tissue was then fixed overnight in 4% paraformaldehyde and placed in ascending sucrose solutions (10%, 20% and 30%). Serial coronal sections (100μm thick) were cut using a Leica microtome (VT1000 S), collected in PBS and stored at 4°C. Free-floating sections were blocked for 1 hour at room temperature in blocking buffer (PBS with 0.02% sodium azide, 0.3% BSA, 0.3% Triton X-100, and 8% serum of the species corresponding to the secondary antibody), and then incubated overnight at 4°C in blocking buffer with the following primary antibodies: mouse anti-MBP (Covance Research Products Inc Cat# SMI-94R-100, RRID:AB_510039) 1:500, rabbit anti-Parvalbumin (Swant Cat# PV27, RRID:AB_2631173) 1:500, and rat anti-RFP (ChromoTek Cat# 5f8-100, RRID:AB_2336064) 1:500. Secondary antibody labeling was performed at room temperature for 2 hours as follows: FITC-conjugated goat anti-mouse IgG (H+L) (Jackson ImmunoResearch Labs Cat# 115-096-003, RRID:AB_2338607) 1:200, Cy5-conjugated goat anti-rabbit IgG (H+L) (Jackson ImmunoResearch Labs Cat# 111-165-144, RRID:AB_2338006) 1:200, and Cy3 goat anti-rat (H + L) (Jackson ImmunoResearch Labs Cat# 112-165-143, RRID:AB_2338250) 1:200. Sections were mounted using ProLong Gold (Invitrogen P36930). Confocal imaging was performed on a Zeiss LSM 880 with Airyscan microscope using three different lasers: FITC (488 nm laser line excitation; 522/35 emission filter), Cy3 (558 nm excitation; 583 emission), and Cy5 (647 excitation; 680/32 emission). The visual cortex was first identified using a 10x objective and imaged using a 63x objective with a z step size of 0.5μm.

Neuronal tracing and analysis of fluorescence images—For tracing of neurons from confocal images, z-stacks were loaded into VAST (Volume Annotation and Segmentation Tool) (Kasthuri et al., 2015). For the quantification of the number of PV^+ and Sst^+ cells with myelinated axons at P30 and P60, we restricted our tracing to cells in layer II/III due to the high density of myelin sheaths in the lower layers of the cortex. To quantify the length of myelinated axon, connected-components analysis was used to identify all spatially separate segments. Next, for each axon object, we found the two most distant points by 3D-filling the object from a random seed point and finding the voxel which is filled last (endpoint 1) and then filling again using endpoint 1 as seed to find the voxel which

is filled last (endpoint 2). This method worked reliably for our objects, which have an elongated tubular shape with no branches (since branches were labeled as separate objects). The filling algorithm also stores the rectilinear distance (1-norm) to the seed point for each voxel of the object. These distances are then used to compute an approximated center line (as a linear list of nodes connected by edges) for each object. This was done by starting at endpoint 1, and using a distance counter d, which was initialized with 0 and increased by 10 (voxels) in each step until the distance of endpoint 2 was reached. For each step a node location was computed by averaging the location of all voxels with distance d from endpoint 1. The total length of each object was computed by summing the Euclidian distances (scaled by the voxel dimensions) between nodes along the center line. Since each axon object has an associated type, we can sum the segment lengths by type and compute the total labeled axon length, myelinated axon length, and percentage myelinated. The global rotation of the tissue in the stack and depth below the pia was computed by manual labeling of the pia and automatic extraction of its location and orientation in the image stack. For the quantification of the total length of myelin segments along the axons of PV^+ and Sst^+ cells, we excluded the axon initial segment (AIS) from our analysis.

Neuronal tracing and rendering of EM data—Neuronal and glial cell bodies and processes were manually traced from a high-resolution EM dataset of an adult (P60-150) animal (Bock et al., 2011) (available online at https://neurodata.io/data/bock11/), accessed in VAST (Berger et al., 2018) as previously described (Tomassy et al., 2014). Briefly, all the cell bodies, axons, and myelin sheaths were labeled manually throughout the EM image stack. The labeled images and meta-data containing the labels were exported and processed externally, or accessed through the VAST API. For rendering of all the traced images, 3D surface meshes of labeled objects were generated from VAST using VastTools (written in Matlab) and imported into 3D Studio Max (Autodesk Inc.) to generate 3D renderings of all the traced objects.

Oligodendrocyte tracing—Tracing of oligodendrocytes and myelinated axons was achieved by identifying the cell bodies of oligodendrocytes throughout the EM dataset. The processes of the oligodendrocytes were subsequently traced until they myelinated an axon. Not all oligodendrocyte processes could be traced to a myelinated axon, either due to the process leaving the V1 EM volume or because the quality of the EM data precluded further tracing.

Interneuron subtype classification—Interneurons were classified according to the following morphological and synaptic connectivity features. Martinotti cell: (1) an ovoid shaped cell soma with a partially myelinated axon projecting from the primary dendrite ascending into layer I, (2) dendrites with sparsely distributed spines which also receive multiple shaft synapses, and (3) an axon forming multiple axon-dendritic symmetrical synapses. Basket cells: (1) an ovoid cell soma, (2) an axon ascending from the soma which is extensively myelinated, (3) aspiny dendrites receiving multiple shaft synapses, and (4) axons forming axo-somatic symmetrical synapses with pyramidal neurons. Bitufted cells: (1) thin unmyelinated axon arising from the base of the soma, which arborizes into the upper layer and lower layers of the cortex, (2) dendrites that are aspiny and receive multiple shaft

synapses, and (3) axon forming axo-dendritic symmetrical synapses. Bipolar cells: (1) small ovoid shape cell body, (2) thin unmyelinated axon emanating from the primary dendrite and projecting to the lower layers of the cortex, (3) aspiny dendrites receiving multiple shaft synapses, and (4) axons forming multiple axo-dendritic symmetrical synapses. Neurogliaform cells: (1) ovoid cell body, (2) thin axon originating from the cell soma arborizing into layer I, (3) dendrites are a spiny and receive multiple shaft synapses, and (3) axon forming multiple axo-dendritic symmetrical synapses (De Marco Garcia et al., 2015; DeFelipe et al., 1986; Markram et al., 2004; Wang et al., 2004).

Axon classification—Axons were classified as either inhibitory or excitatory using previously established criteria (Bock et al., 2011; del Rio and DeFelipe, 1997; Micheva et al., 2016; Wang et al., 2004). Axons which could be traced back to cell bodies could be easily classified by cell body morphology and appearance of dendrites at some distance from the cell body (many spines receiving asymmetric synapses for excitatory cells vs. numerous shaft synapses and relative spinelessness for inhibitory cells). Axons which we could not trace to the cell bodies were classified using previously established methods for the identification of symmetrical and asymmetrical synapses (Bock et al., 2011).

Identification of locally available myelinated axons surrounding oligodendrocytes 2 and 5.—To quantify the total number of locally available myelinated axons surrounding oligodendrocyte 2 and 5, we first found the maximal reach of oligodendrocyte branches in all six cardinal directions in the data set and used these to define boundary boxes surrounding the oligodendrocytes (Figure 5D). We then traced all of the axons within both boundary boxes and attempted to classify them as excitatory and inhibitory as described above. We could not classify 21% of axons surrounding oligodendrocyte 2 and 20% of axons surrounding oligodendrocyte 4 as either inhibitory or excitatory because they did not connect to a cell body and did not make enough reliably identifiable synapses within the dataset.

Identification of receptor ligand interactions—In order to identify subtype-specific molecules implicated in PV-Oligodendrocyte interaction, we identified genes whose average gene expression in PV^+ interneurons was greater than two-fold higher compared to VIP^+ or $nNOS^+$ interneurons, using a previously published dataset (GSE: 71585; Tasic et al., 2016). The aim of this bioinformatic analysis was to test whether highly-myelinated PV^+ neurons differentially expressed ligands for oligodendrocyte receptors, compared to less-myelinated interneuron classes. We refined this gene list based on their biological function to include only extracellular matrix, secretory and surface proteins, since these genes would most likely play a role in cell-cell interaction, using gene lists from MIT's Matrisome Project (http://web.mit.edu/hyneslab/matrisome/) (Naba et al., 2012). We obtained a list of genes enriched across all oligodendrocyte populations (Marques et al., 2016). We compared the gene lists to the interactome database StringDB (https://string-db.org/) to computationally annotate possible ligand receptor pairs across the two cell types, by first identifying all potential ligands in PV^+ cells and then using StringDB to identify receptors/interacting partners expressed by oligodendrocytes.

QUANTIFICATION AND STATISTICAL ANALYSIS

Data presentation and statistical analysis—The summary data are presented in the text as mean and s.e.m. from n cells or animals. Comparisons involving two data sets only were performed using a two-sided Welch two-sample t- test that does not assume equal variance. Analyses that involved data from three or more groups were performed using one-way or two-way analysis of variance (Welch heteroscedastic F test) that was followed by pairwise comparisons using two-sided Welch two-sample t tests (with Holm's sequential Bonferroni correction for multiple comparisons). Binomial distribution analysis were carried out using Matlab 2016. Differences were considered significant at * $P < 0.05$, ** $P < 0.01$, and *** $P < 0.001$. Statistical tests were performed using Prism version 7.0c (GraphPad Software, Inc) or MATLAB 2016 (The MathWorks Inc., Natick, MA).

Supplementary Material

Refer to Web version on PubMed Central for supplementary material.

Acknowledgments

We are grateful to Juliana Brown and members of the Arlotta and Lichtman laboratories for insightful discussions and reading of the manuscript, and to Dennis Sun for designing the graphical abstract. We are thankful to Wendy Macklin and Lisa Goodrich for sharing the Plp1-eGFP mouse and to Davi Bock and Clay Reid for making the EM dataset available. This work was supported by grants from the Stanley Center for Psychiatric Research at the Broad Institute of MIT and Harvard to P.A. and J.W.L., and the NIH (R01 NS078164 and Conte Center) to P.A. J.W.L. acknowledges support by IARPA, NIH Conte Center and the MURI Army Research Office. During the course of the work P.A. was a New York Stem Cell Foundation Robertson Investigator.

References

Arlotta P, Molyneaux BJ, Chen J, Inoue J, Kominami R, and Macklis JD (2005). Neuronal subtype-specific genes that control corticospinal motor neuron development in vivo. Neuron 45, 207–221. [PubMed: 15664173]

Berger DR, Seung HS, and Lichtman JW (2018). VAST (Volume Annotation and Segmentation Tool): Efficient Manual and Semi-Automatic Labeling of Large 3D Image Stacks. Front Neural Circuits 12, 88. [PubMed: 30386216]

Bock DD, Lee WC, Kerlin AM, Andermann ML, Hood G, Wetzel AW, Yurgenson S, Soucy ER, Kim HS, and Reid RC (2011). Network anatomy and in vivo physiology of visual cortical neurons. Nature 471, 177–182. [PubMed: 21390124]

Butt AM, Ibrahim M, and Berry M (1998). Axon-myelin sheath relations of oligodendrocyte unit phenotypes in the adult rat anterior medullary velum. J Neurocytol 27, 259–269. [PubMed: 10640184]

Czopka T, Ffrench-Constant C, and Lyons DA (2013). Individual oligodendrocytes have only a few hours in which to generate new myelin sheaths in vivo. Dev Cell 25, 599–609. [PubMed: 23806617]

De Marco Garcia NV, Priya R, Tuncdemir SN, Fishell G, and Karayannis T (2015). Sensory inputs control the integration of neurogliaform interneurons into cortical circuits. Nat Neurosci 18, 393–401. [PubMed: 25664912]

DeFelipe J, Hendry SH, and Jones EG (1986). A correlative electron microscopic study of basket cells and large GABAergic neurons in the monkey sensory-motor cortex. Neuroscience 17, 991–1009. [PubMed: 2423922]

DeFelipe J, Lopez-Cruz PL, Benavides-Piccione R, Bielza C, Larranaga P, Anderson S, Burkhalter A, Cauli B, Fairen A, Feldmeyer D, et al. (2013). New insights into the classification and nomenclature of cortical GABAergic interneurons. Nat Rev Neurosci 14, 202–216. [PubMed: 23385869]

del Rio MR, and DeFelipe J (1997). Synaptic connections of calretinin-immunoreactive neurons in the human neocortex. J Neurosci 17, 5143–5154. [PubMed: 9185552]

Friedman B, Hockfield S, Black JA, Woodruff KA, and Waxman SG (1989). In situ demonstration of mature oligodendrocytes and their processes: an immunocytochemical study with a new monoclonal antibody, rip. Glia 2, 380–390. [PubMed: 2530173]

Gibson EM, Purger D, Mount CW, Goldstein AK, Lin GL, Wood LS, Inema I, Miller SE, Bieri G, Zuchero JB, et al. (2014). Neuronal activity promotes oligodendrogenesis and adaptive myelination in the mammalian brain. Science 344, 1252304. [PubMed: 24727982]

GraphPad. GraphPad Software, La Jolla California USA.

Hu H, Cavendish JZ, and Agmon A (2013). Not all that glitters is gold: off-target recombination in the somatostatin-IRES-Cre mouse line labels a subset of fast-spiking interneurons. Front Neural Circuits 7, 195. [PubMed: 24339803]

Inan M, and Anderson SA (2014). The chandelier cell, form and function. Curr Opin Neurobiol 26, 142–148. [PubMed: 24556285]

Jiang X, Shen S, Cadwell CR, Berens P, Sinz F, Ecker AS, Patel S, and Tolias AS (2015). Principles of connectivity among morphologically defined cell types in adult neocortex. Science 350, aac9462. [PubMed: 26612957]

Kasthuri N, Hayworth KJ, Berger DR, Schalek RL, Conchello JA, Knowles-Barley S, Lee D, Vazquez-Reina A, Kaynig V, Jones TR, et al. (2015). Saturated Reconstruction of a Volume of Neocortex. Cell 162, 648–661. [PubMed: 26232230]

Madisen L, Zwingman TA, Sunkin SM, Oh SW, Zariwala HA, Gu H, Ng LL, Palmiter RD, Hawrylycz MJ, Jones AR, et al. (2010). A robust and high-throughput Cre reporting and characterization system for the whole mouse brain. Nat Neurosci 13, 133–140. [PubMed: 20023653]

Mallon BS, Shick HE, Kidd GJ, and Macklin WB (2002). Proteolipid promoter activity distinguishes two populations of NG2-positive cells throughout neonatal cortical development. J Neurosci 22, 876–885. [PubMed: 11826117]

Markram H, Toledo-Rodriguez M, Wang Y, Gupta A, Silberberg G, and Wu C (2004). Interneurons of the neocortical inhibitory system. Nat Rev Neurosci 5, 793–807. [PubMed: 15378039]

Marques S, Zeisel A, Codeluppi S, van Bruggen D, Mendanha Falcao A, Xiao L, Li H, Haring M, Hochgerner H, Romanov RA, et al. (2016). Oligodendrocyte heterogeneity in the mouse juvenile and adult central nervous system. Science 352, 1326–1329. [PubMed: 27284195]

Martin KA, and Whitteridge D (1984). Form, function and intracortical projections of spiny neurones in the striate visual cortex of the cat. J Physiol 353, 463–504. [PubMed: 6481629]

McGee AW, Yang Y, Fischer QS, Daw NW, and Strittmatter SM (2005). Experience-driven plasticity of visual cortex limited by myelin and Nogo receptor. Science 309, 2222–2226. [PubMed: 16195464]

Micheva KD, Wolman D, Mensh BD, Pax E, Buchanan J, Smith SJ, and Bock DD (2016). A large fraction of neocortical myelin ensheathes axons of local inhibitory neurons. Elife 5.

Naba A, Clauser KR, Hoersch S, Liu H, Carr SA, and Hynes RO (2012). The matrisome: in silico definition and in vivo characterization by proteomics of normal and tumor extracellular matrices. Mol Cell Proteomics 11.

Peters A (1990). The axon terminals of vasoactive intestinal polypeptide (VIP)-containing bipolar cells in rat visual cortex. J Neurocytol 19, 672–685. [PubMed: 2077110]

Peters A, and Proskauer CC (1980). Smooth or sparsely spined cells with myelinated axons in rat visual cortex. Neuroscience 5, 2079–2092. [PubMed: 7465047]

Petilla Interneuron Nomenclature Group, Ascoli GA, Alonso-Nanclares L, Anderson SA, Barrionuevo G, Benavides-Piccione R, Burkhalter A, Buzsaki G, Cauli B, Defelipe J, et al. (2008). Petilla terminology: nomenclature of features of GABAergic interneurons of the cerebral cortex. Nat Rev Neurosci 9, 557–568. [PubMed: 18568015]

Remahl S, and Hildebrand C (1990). Relations between axons and oligodendroglial cells during initial myelination. II. The individual axon. J Neurocytol 19, 883–898. [PubMed: 2292718]

Rudy B, Fishell G, Lee S, and Hjerling-Leffler J (2011). Three groups of interneurons account for nearly 100% of neocortical GABAergic neurons. Dev Neurobiol 71, 45–61. [PubMed: 21154909]

Schmidt H, Gour A, Straehle J, Boergens KM, Brecht M, and Helmstaedter M (2017). Axonal synapse sorting in medial entorhinal cortex. Nature 549, 469–475. [PubMed: 28959971]

Shannon P, Markiel A, Ozier O, Baliga NS, Wang JT, Ramage D, Amin N, Schwikowski B, and Ideker T (2003). Cytoscape: a software environment for integrated models of biomolecular interaction networks. Genome Res 13, 2498–2504. [PubMed: 14597658]

Stedehouder J, Couey JJ, Brizee D, Hosseini B, Slotman JA, Dirven CMF, Shpak G, Houtsmuller AB, and Kushner SA (2017). Fast-spiking Parvalbumin Interneurons are Frequently Myelinated in the Cerebral Cortex of Mice and Humans. Cereb Cortex 27, 5001–5013. [PubMed: 28922832]

Taniguchi H, He M, Wu P, Kim S, Paik R, Sugino K, Kvitsiani D, Fu Y, Lu J, Lin Y, et al. (2011). A resource of Cre driver lines for genetic targeting of GABAergic neurons in cerebral cortex. Neuron 71, 995–1013. [PubMed: 21943598]

Tasic B, Menon V, Nguyen TN, Kim TK, Jarsky T, Yao Z, Levi B, Gray LT, Sorensen SA, Dolbeare T, et al. (2016). Adult mouse cortical cell taxonomy revealed by single cell transcriptomics. Nat Neurosci 19, 335–346. [PubMed: 26727548]

The MathWorks, Inc. MATLAB 8.0 and Statistics Toolbox 8.1 (Natick, Massachusetts, United States.).

Tomassy GS, Berger DR, Chen HH, Kasthuri N, Hayworth KJ, Vercelli A, Seung HS, Lichtman JW, and Arlotta P (2014). Distinct profiles of myelin distribution along single axons of pyramidal neurons in the neocortex. Science 344, 319–324. [PubMed: 24744380]

Wang Y, Toledo-Rodriguez M, Gupta A, Wu C, Silberberg G, Luo J, and Markram H (2004). Anatomical, physiological and molecular properties of Martinotti cells in the somatosensory cortex of the juvenile rat. J Physiol 561, 65–90. [PubMed: 15331670]

Watkins TA, Emery B, Mulinyawe S, and Barres BA (2008). Distinct stages of myelination regulated by gamma-secretase and astrocytes in a rapidly myelinating CNS coculture system. Neuron 60, 555–569. [PubMed: 19038214]

Yavorska I, and Wehr M (2016). Somatostatin-Expressing Inhibitory Interneurons in Cortical Circuits. Front Neural Circuits 10, 76. [PubMed: 27746722]

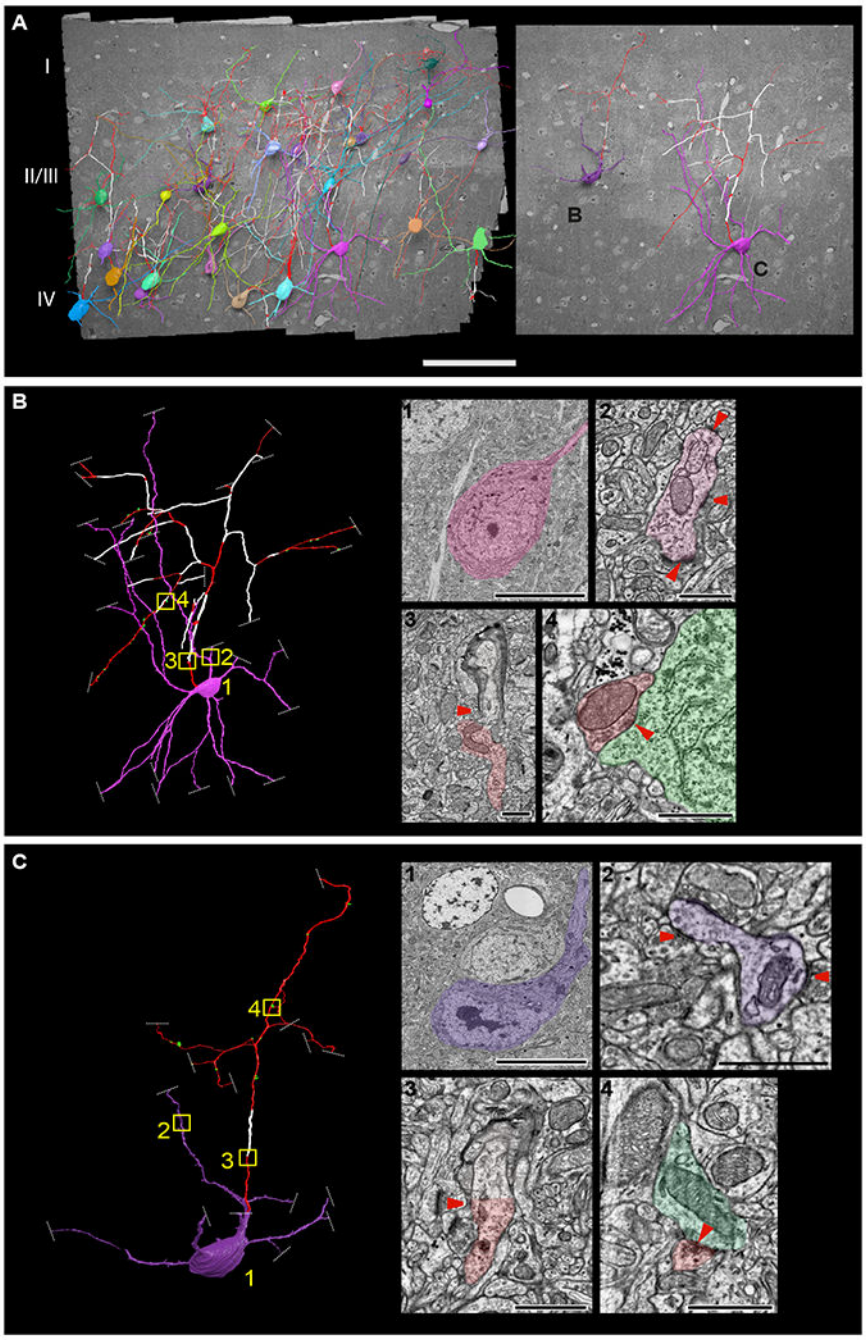

Figure 1. Cortical interneurons develop class-specific myelination patterns

(**A**) 3D reconstructions of 28 neurons from a high-resolution EM dataset of mouse V1 cortex (Bock et al., 2011), displaying non-myelinated axons (red) and myelinated axons (white). Scale bar 100μm. Image to the right are 3D renderings of two neurons with distinctive morphological features of a cortical basket cell (**B**) and cortical Martinotti cell (**C**). **(B, C)** Close-up renderings of these two cells. Images to the right are representative single EM sections of (1) cell bodies, (2) dendrites with a sparse number of spines receiving multiple shaft synapses, (3) myelinating ascending axon, and (4) axons forming symmetrical

synapses (red) with the postsynaptic cell body labeled in green (red arrowheads indicate the location of axons, synapses onto dendrites, and asymmetrical synapses). Boxed regions on the 3D rendered images (yellow) indicate the location corresponding to the EM images. Dashed white lines indicate the end of EM tracing due to the axon or dendrites leaving the V1 EM volume, or the quality of the EM data precluding further tracing. Scale bars, 10μm for panel 1 and 1μm for panels 2–4. See also Figures S1 and S2 and Table S1.

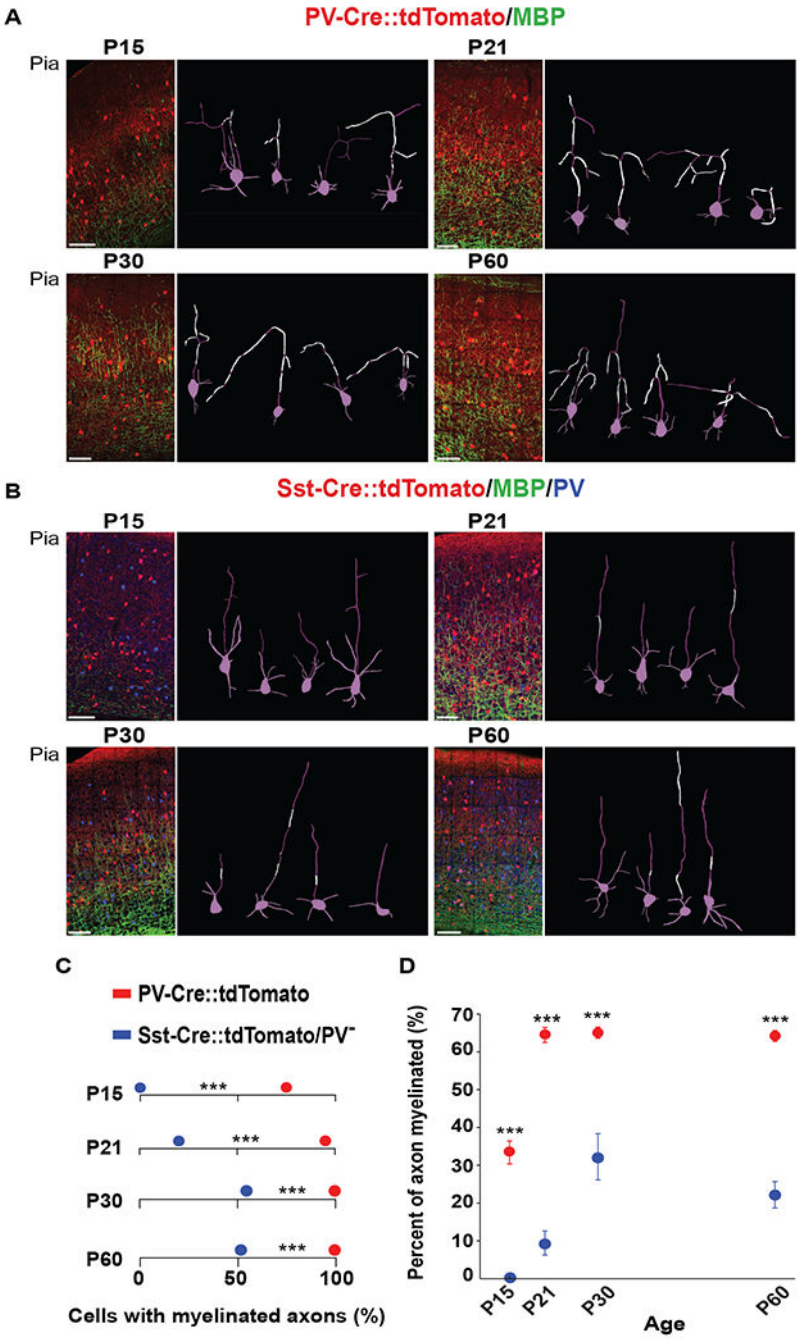

Figure 2. Interneuron class-specific myelination patterns are present from the onset of myelination

(A-B) Representative confocal images from the V1 of PV::tdTomato (red) and Sst::tdTomato (red) mice at P15, P21, P30 and P60, labeled with anti-MBP (green). Sst::tdTomato mice were additionally labeled with anti-PV (blue) to exclude PV^+/Sst^+ cells. Images to the right of each panel are example 3D reconstructions of traced neurons with myelinated segments in white and cell bodies, dendrites and non-myelinated axons in magenta. Scale bar 100μm.

(C) Pooled data showing the number of PV^+ (PV::tdTomato) cells with myelinated axons

compared to Sst^+/PV^- cells (Sst::tdTomato) at P15, P21, P30 and P60. *** $P < 0.001$, (Fisher's exact test); (n=3 animals). **(D)** Pooled data showing the higher percentage of myelin coverage along individually traced PV^+ cell axons compared to Sst^+/PV^- axons at each age. Data are presented as mean ± s.e.m. *** $P < 0.001$ (unpaired Welch two-sample *t* tests). See also Figure S3 and Table S2.

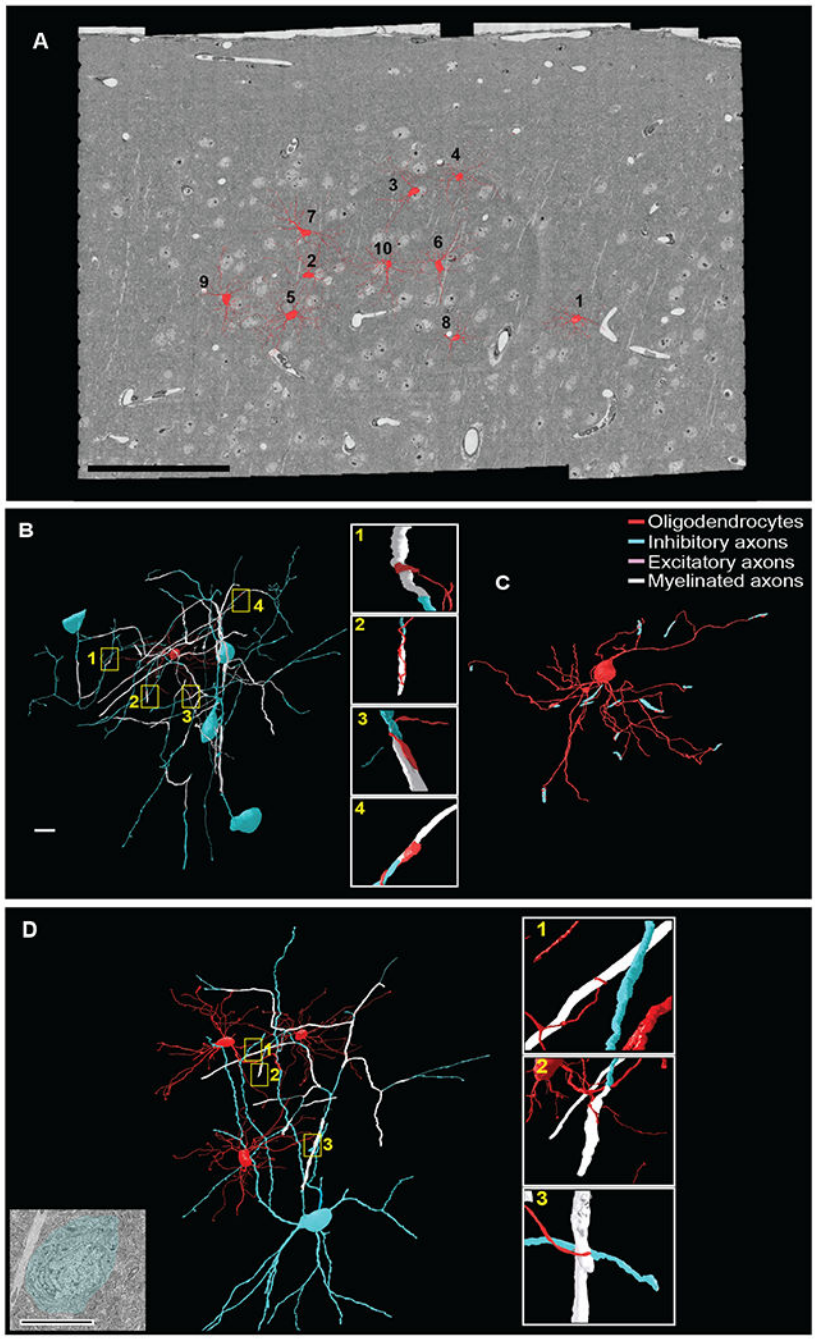

Figure 3. Identification of oligodendrocytes in the mouse visual cortex and their myelinating contacts

(**A**) 3D reconstructions of 10 oligodendrocytes located in layer II/III of the mouse visual cortex (red). Scale bar 100μm. (**B**) 3D reconstruction of a single oligodendrocyte (Oligodendrocyte 4, Figure 3A **and** Figure 5A) myelinating the axons of multiple inhibitory neurons. Yellow boxed regions correspond to the four myelinating contacts with inhibitory axons shown in enlargements at right. (**C**) 3D reconstruction of the oligodendrocyte 4 (red) and its myelinating contacts with inhibitory axons (blue). Scale bar 10μm. (**D**) 3D renderings

of three oligodendrocytes myelinating the axons of the same cortical interneuron. Yellow boxed regions correspond to the oligodendrocyte processes ensheathing axons of inhibitory cells enlarged at right. EM image at far left shows the cell body of the myelinated interneuron. Scale bar 10μm. (**B, D**) The oligodendrocyte and all branches are labeled in red; neuronal cell soma, dendrites and non-myelinated axon in blue; and myelinated axons in white.

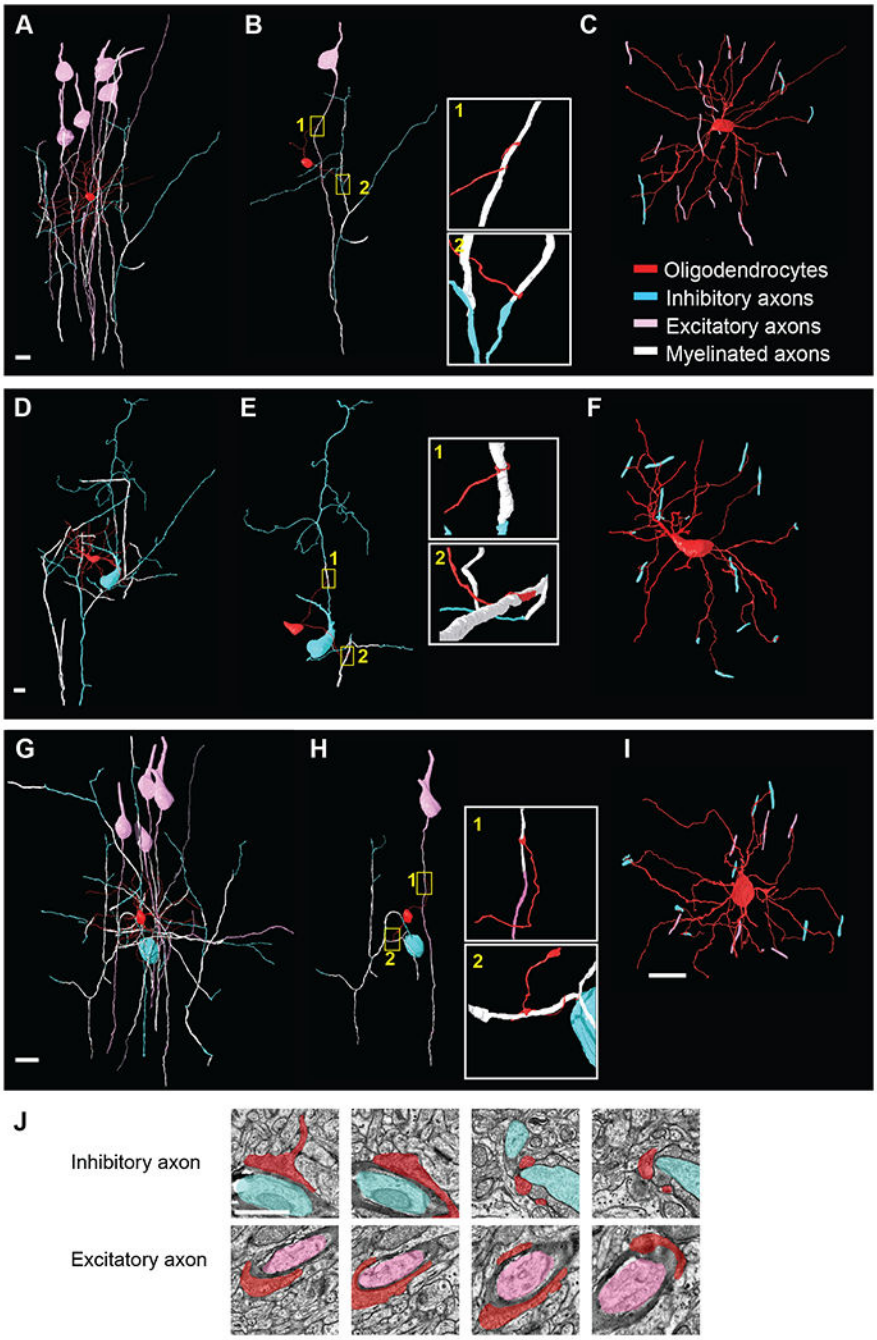

Figure 4. Subpopulations of cortical oligodendrocytes show individual bias towards myelinating the axons of inhibitory neurons

(**A-I**) 3D reconstruction of oligodendrocyte 2 (**A-C**, predominantly myelinating axons of excitatory neurons), oligodendrocyte 7 (**D-F,** myelinating multiple axons of inhibitory neurons) and oligodendrocyte 10 (**G-I** myelinating both excitatory and inhibitory neurons) from the Bock et al. EM dataset (Figure 3A **and** Figure 5A). The oligodendrocytes are labeled in red, myelinated axons in white, inhibitory soma and non-myelinated axons in blue, and excitatory soma and non-myelinated axon in pink. (**B, E, H**) Reconstructions of

two of the oligodendrocytes' processes myelinating the axon of a target excitatory or inhibitory neuron. Boxed images to the right are enlargements of two individual processes ensheathing the target axons. (**C, F, I**) 3D reconstruction of the oligodendrocyte showing all myelinating contacts with excitatory (pink) and inhibitory axons (blue). Scale bar 10μm. (**J**) Representative EM images of two processes projecting from oligodendrocyte 10 (red) myelinating individual inhibitory (blue) and excitatory (pink) axons. Scale bar 1μm. See also Figures S4 and S5 and Table S1.

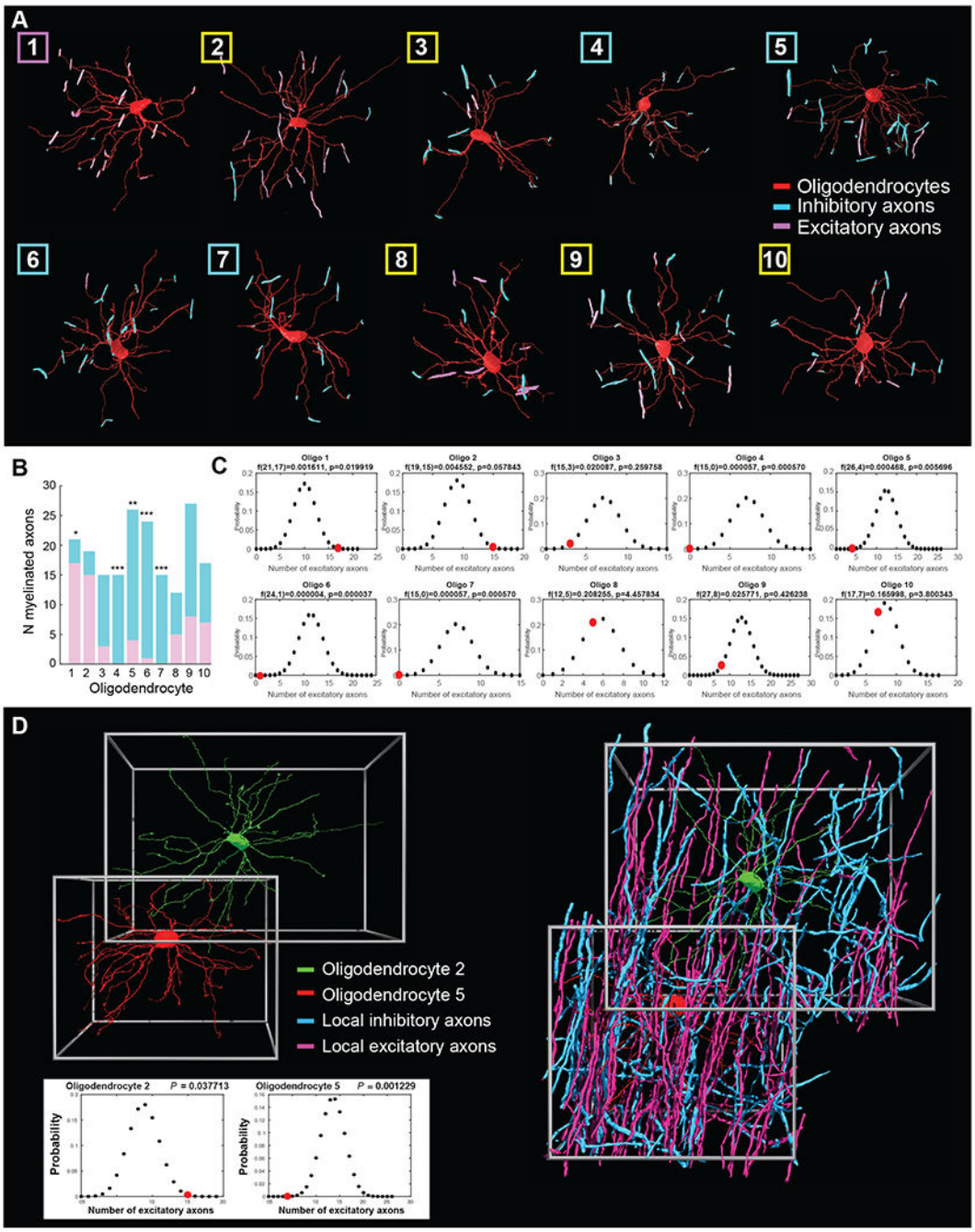

Figure 5. Oligodendrocyte bias towards excitatory versus inhibitory axons is independent of the availability of surrounding excitatory and inhibitory axons

(**A**) 3D renderings of 10 oligodendrocytes located in layer II/III of the visual cortex myelinating multiple inhibitory (blue) and excitatory axons (pink). Box color denotes bias towards excitatory (pink) or inhibitory (blue) axons, or no bias (yellow). (**B**) Graph representing the total number of inhibitory (blue) and excitatory (purple) axons myelinated by each of the 10 traced oligodendrocytes in layer II/III, with asterisks indicating oligodendrocytes where the ratio is significantly different from expected at random. * $P <$

0.05, ** $P < 0.01$, *** $P < 0.001$ (binomial distribution analysis, see Methods and Figure S5). (**C**) Binomial distribution plots for the 10 oligodendrocytes, comparing the total number of excitatory axons myelinated by each oligodendrocyte (red circles) to the number expected from the ratio of inhibitory and excitatory axons (48% inhibitory and 52% excitatory). (**D**) Individual oligodendrocytes show bias towards different axon types independent of local axon availability. Left, 3D rendering of oligodendrocytes 2 (green) and 5 (red) demonstrating their proximity and multiple overlapping processes. Right, 3D reconstruction of these cells with all surrounding myelinated axons whose type could be identified; myelinated excitatory axons (pink) and myelinated inhibitory axons (blue). Bottom: binomial distribution plots for oligodendrocyte 2 and 5, comparing the actual number of myelinated excitatory axons (red circles) with the number expected from the average ratio of locally available classifiable myelinated axons (Oligodendrocyte 5: 52% excitatory and 48% inhibitory axons; Oligodendrocyte 2: 46.2% excitatory and 53.8% inhibitory axons). See also Figure S5.